International Journal of Remote Sensing

ISSN: (Print) (Online) Journal homepage: https://www.tandfonline.com/loi/tres20

Design of supercontinuum laser hyperspectral light detection and ranging (LiDAR) (SCLaHS LiDAR)

Guoqing Zhou, Xiang Zhou, Youjian Song, Donghui Xie, Long Wang, Guangjian Yan, Minglie Hu, Bowen Liu, Weidong Shang, Chenghu Gong, Cheng Wang, Huaguo Huang, Yiqiang Zhao, Zhigang Liu, Guangyun Zhang, Xing Wang, Sheng Nie, Mao Ye, Songlin Liu, Qiaofeng Tan, Ke Li, Fengyuan Wei, Wei Su, Jinshou Tian, Qingkang Ai, Lvyun Yang, Bo Song, Jiasheng Xu, Lieping Zhang, Wei Li, Ruirui Wang, Hao Xue, Hao Dong, Ying Yu & Hongtao Wang

To cite this article: Guoqing Zhou, Xiang Zhou, Youjian Song, Donghui Xie, Long Wang, Guangjian Yan, Minglie Hu, Bowen Liu, Weidong Shang, Chenghu Gong, Cheng Wang, Huaguo Huang, Yiqiang Zhao, Zhigang Liu, Guangyun Zhang, Xing Wang, Sheng Nie, Mao Ye, Songlin Liu, Qiaofeng Tan, Ke Li, Fengyuan Wei, Wei Su, Jinshou Tian, Qingkang Ai, Lvyun Yang, Bo Song, Jiasheng Xu, Lieping Zhang, Wei Li, Ruirui Wang, Hao Xue, Hao Dong, Ying Yu & Hongtao Wang (2021) Design of supercontinuum laser hyperspectral light detection and ranging (LiDAR) (SCLaHS LiDAR), International Journal of Remote Sensing, 42:10, 3731-3755, DOI: 10.1080/01431161.2021.1880662

To link to this article: https://doi.org/10.1080/01431161.2021.1880662

INTERNATIONAL JOURNAL OF REMOTE SENSING
2021, VOL. 42, NO. 10, 3731–3755
https://doi.org/10.1080/01431161.2021.1880662

Taylor & Francis
Taylor & Francis Group

Design of supercontinuum laser hyperspectral light detection and ranging (LiDAR) (SCLaHS LiDAR)

Guoqing Zhou[a,b,c], Xiang Zhou[a,b,c], Youjian Song[d], Donghui Xie[e], Long Wang[f], Guangjian Yan[e], Minglie Hu[d], Bowen Liu[d], Weidong Shang[g], Chenghu Gong[f], Cheng Wang[h], Huaguo Huang[i], Yiqiang Zhao[a], Zhigang Liu[e], Guangyun Zhang[b], Xing Wang[j], Sheng Nie[h], Mao Ye[a], Songlin Liu[k], Qiaofeng Tan[l], Ke Li[m], Fengyuan Wei[n], Wei Su[o], Jinshou Tian[p], Qingkang Ai[p], Lvyun Yang[q], Bo Song[f], Jiasheng Xu[f], Lieping Zhang[f], Wei Li[f], Ruirui Wang[i], Hao Xue[f], Hao Dong[m], Ying Yu[k] and Hongtao Wang[n]

[a]School of Microelectronics, Tianjin University, Tianjin, China; [b]The Center of Remote Sensing, Tianjin University, Tianjin, China; [c]Guangxi Key Laboratory for Spatial Information and Geomatics, Guilin University of Technology, Guilin, China; [d]School of Precision Instrument and Optoelectronics Engineering, Tianjin University, Tianjin, China; [e]Institute of Remote Sensing Science and Engineering, Beijing Normal University, Beijing, China; [f]Changchun Institute of Optics, Fine Mechanics and Physics, Chinese Academy of Science, Changchun, China; [g]Beijing Institute of Space Mechanics and Electricity, China Academy of Space Technology, Beijing, China; [h]Institute of Remote Sensing and Digital Earth, Chinese Academy of Sciences, Beijing, China; [i]Department of Forestry, The College of Forestry of Beijing Forestry University, Beijing, China; [j]Xi'an Institute of Optics and Precision Mechanics, Chinese Academy of Sciences, Xi'an, China; [k]School of Spatial Geographic Information, National Digital Switching System Engineering and Technology R&D Center, Zhengzhou, China; [l]Department of Precision Instruments, Tsinghua University, Beijing, China; [m]Tianjin Jinhang Institute of Technology Physics, China Aerospace Science and Industry Co., Ltd, Tianjin, China; [n]School of Surveying and Land Information Engineering, Henan Polytechnic University, Jiaozuo, China; [o]College of Land Science and Technology, China Agricultural University, Beijing, China; [p]Department of Product Research and Development, Beijing Laize Photoelectric Technology Co., Ltd, Beijing, China; [q]Wuhan National Laboratory for Optoelectronics, Huazhong University of Science and Technology, Wuhan, China

ABSTRACT

Traditional Light Detection and Rangings (LiDARs) can quickly collect high-accuracy of three-dimensional (3D) point cloud data at a designated wavelength (i.e., cannot obtain hyperspectral data), while the passive hyperspectral imager can collect rich spectral data of ground objects, but are lack of 3D spatial data. This paper presents one innovative study on the design of airborne-oriented supercontinuum laser hyperspectral (SCLaHS) LiDAR with 50 bands covering 400 nm to 900 nm at a spectral resolution of 10 nm and ground sampling distance (GSD) of 0.5 m. The major innovations include (1) development of the high-power narrow-pulse supercontinuum laser source covering 400 nm to 900 nm with 50 bands using multi-core microstructure fibre, all-polarization maintaining fibre and ultra-long cavity structure, (2) a miniaturized aberration correction holographic concave grating spectroscopic and streak tube technique are developed for 50 bands laser echoes

ARTICLE HISTORY
Received 17 July 2020
Accepted 31 December 2020

CONTACT Guoqing Zhou 1227416902@qq.com School of Microelectronics, Tianjin University, Tianjin 300072, China

detection at high spectral-spatial-temporal resolution and dynamic airborne platform, and (3) the algorithm theoretic basis for SCLaHS LiDAR point cloud data 3D geodetic coordination calculation, including in-flight airborne calibration algorithm. The initial experimental results demonstrated that the designed SCLaHS LiDAR is doable, and a prototype of the (SCLaHS) LiDAR intends to be implemented.

1. Background

The Ministry of Science and Technology (MOST) of China in 2018 made an announcement, entitled 'All-day active hyperspectral Light Detection and Ranging (LiDAR) imaging technology'. This Research Announcement is the MOST of China umbrella solicitation, entitled 'National Key Research and Development Plan at Earth Observation and Navigation'. The purpose of this Call for Proposal (CFP) is to develop an airborne-oriented supercontinuum laser hyperspectral LiDAR (hereafter called '*SCLaHS LiDAR*') system for observation of the three-dimensional (3D) structure and the spectral information of the targeted grounds, to advance China's hyperspectral LiDAR imaging technology, even to lead laser hyperspectral remote sensing imaging and its applications in China and even international community.

The SCLaHS LiDAR system is specified as an airborne-oriented supercontinuum laser light source-based ranging and hyperspectral full-wave synchronous imaging at spectral range of 400 nm to 900 nm at a spectral resolution of 10 nm, and with a ground sampling distance (GSD) of 0.5 m, i.e., the target's laser hyperspectral echo spectral and 3D ranging data are synchronously collected. The specifications of the prototype of SCLaHS LiDAR are:

Spectral range: 400 nm to 900 nm,
The spectral resolution: ≥ 10 nm,
Number of bands: ≥ 50,
Quantization for laser echo: 12 bits,
Detection distance: ≥ 500 m,
Field of view: ≥ 30°,
Size of the laser footprint: ≤ 0.1 mrad,
Ground sample distances: ≤ 1 mrad,
Ranging resolution: ≤ millimetre level, and
Average spectral power density: ≥ 15 mW nm^{-1}.

For the reasons above, a research team, consisting of five research groups (GPs), from universities, the Chinese Academy of Sciences, and the Aerospace Science and Technology Corporation, was organized. The team members with various research backgrounds at China's top research affiliations in the fields of sensor development, data processing, and remote sensing applications get together to resolve the key techniques.

2. Review of relevant work

Traditional LiDARs can quickly obtain high-accuracy of three-dimensional (3D) point cloud data of ground objects, but are often limited to a specific wavelength (i.e., cannot obtain hyperspectral data). Although the existing hyperspectral imagers can obtain rich spectral information of ground objects, but are lack of 3D spatial information of ground objects. Therefore, the multi-spectral LiDAR in the most current years has considered as a novel remotely sensing technology that uses active laser light sources to simultaneously acquire 3D spatial data and spectral information. This cutting-edge technique has attracted many scientists in remote sensing community (e.g., Zhou and Zhou 2018; Swatantran et al. 2011; Suomalainen et al. 2011). Per the number of bands, they can be categorized into:

(1) *2 bands LiDAR*: Rall and Knox (2004) first proposed a 2 bands LiDAR at the bands of 660 nm and 780 nm to detect objects, respectively. The LiDAR instrument was horizontally operated for measure from a laboratory's rooftop from a stand of deciduous trees far away several hundred metres. The laser power is 30 mW and 70 mW, which correspond to 660 nm and 780 nm bands, respectively. Single photon counting module (SPCM) is adopted to detect the laser signals returned from the trees. Kaasalainen, Lindroos, and Hyyppa (2007) reported a supercontinuum laser light source (SCLLS) with a spectral range from 600 nm to 2000 nm at an average out-put power of 100 mW. Such a type of SCLLS generated by a nonlinear optical fibre make it possible for hyperspectral LiDAR to be manufactured. Chen et al. (2010) presented a multiple spectral LiDAR with 2 bands at 600 nm and 800 nm, respectively. The two APD detectors are used to detect the waveform returned from the target away from 20 metres. This type of LiDAR instrument has been used in the laboratory for research. Douglas et al. (2012) presented a Dual-wavelength echidna LiDAR for ground-based forest scanning. Gaulton et al. (2013) presented the potential of dual-wavelength laser scanning for estimating vegetation moisture content.

(2) *3 bands LiDAR*: Guerrero-Rascado, Ruiz, and Alados-Arboledas (2008) presented a 3 bands LiDAR with the wavelengths of 1064, 532, 355 nm to measure vertical profiles of different aerosol properties, respectively. The LiDAR used one APD detector to detect the echoes at wavelength of 1064 nm and two PMT detectors to detect the echoes from other two wavelengths. The detection mode is both analogue and photon counting. Wirth et al. (2009) presented a LiDAR with high-power laser source at three wavelengths of 935, 1064, and 532 nm. Their detectors adopted are two APDs for 1064 nm and 935 nm, one PMT for 532 nm. Nishizawa, Sugimoto, and Matsui (2011) developed a 4 bands LiDAR, in which an iodine absorption filter was used for 532 nm, a Fabry-Perot etalon is used for 355 nm. One APD detector is used for 1064 nm, and two PMT detectors are used for 532 nm, 355 nm, respectively. Yang et al. (2013) developed a wide-spectral LiDAR for simultaneous detection of multiple toxic gases. The detection errors were analysed and compared through selecting three different near-infrared wavelength bands data ranging from 900 through 1000 nm. The experimental results demonstrated that the three chemical poisons mixed could be identified, and the change trend of the gas concentration can be well tracked. Teledyne Optech (Vaughan, ON, Canada) in 2014 developed the world's first commercial airborne multispectral LiDAR sensor, named 'Optech Titan'. The Optech Titan incorporates 3 independent laser wavelengths (532, 1064, and 1550 nm (0.5/1.0/1.5 microns)) into a single sensor design, with a ground sampling rate of 300 kHz per beam (Teledyne Optech – Titan Brochure and Specifications 2015). Muller et al. (2014) reported their

development on the second generation of high spectral resolution LiDAR. It was operated at laser wavelengths of 355, 532, and 1064 nm and was used for measuring the profiles of particle backscatter coefficients and linear particle depolarization ratios at spectral bands of 355, 532, and 1064 nm, and particle volume extinction coefficients at spectral bands of 355 and 532 nm. Rao et al. (2018) developed a prototype of three-bands LiDAR, in which a solid-state laser was applied as a light source. The laser emitting and receiving subsystems are coaxial. The two PMT detectors are used to receive the signals returned at 355 nm and 532 nm bands, and one APD detector at 1064 nm band. The converted electrical signals are collected by an oscilloscope.

(3) *4 bands LiDAR*: Morsdorf et al. (2009) presented a simulated LiDAR instrument with 4 bands of 531, 550, 670, and 780 nm, respectively. The instrument was designated on airborne-based platform with a flight height of 500 m. Wei et al. (2012) presented a laboratory-based prototype of multispectral LiDAR with 4 bands at a central wavelength of 555, 670, 700, and 780 nm, respectively. Four PMT detectors are used to receive the returned signals at waveforms at 7 m away. Li et al. (2014) and Niu et al. (2015) presented a laboratory-based LiDAR instrument with 4 bands at 531, 570, 670, and 780 nm. Four APD detectors forming an array to receive the signals returned at waveform of approximative 10 m away.

(4) *8 bands LiDAR*: Hakala et al. (2012) firstly used super continuum laser and with 8 channels for potential development of LiDAR. Nevalainen et al. (2014) reported a SCLLS for potential development of LiDAR, whose spectral bands cover from 400 nm to 2200 nm with two 8 bands at 554.8 nm, 623.5 nm, 691.1 nm, 725.5 nm, 760.3 nm, 795.5 nm, 899.0 nm, 1000.4 nm (or 545.0 nm, 641.2 nm, 675.0 nm, 711.0 nm, 741.5 nm, 778.0 nm, 978.0 nm and 1292.4 nm), respectively. The measurements were designated in both indoor and outdoor conditions at about 7 m away. Puttonen et al. (2015), Puttonen et al. (2016)) presented a prototype of from 420 nm to 2100 nm and at the central wavelength of 545.5 nm, 641.2 nm, 675.0 nm, 711.0 nm, 741.5 nm, 778.4 nm, and 978.0 nm. The average output power of laser light source is 41 mW. The LiDAR was validated and tested outdoor and indoor through detecting man-made targets at about 15 m away.

(5) *16 and 32 bands LiDAR*: Hakala et al. (2012) reported a prototype of multi-wavelength LiDAR at a spectral range of 480 nm to 2200 nm and spectral sampling interval of 34 nm. A 1×16 APD array detector was used to convert the spectrally separated laser light to analog voltages. The maximum effective range to be operated is about 20 metres in laboratory circumstance. The average output power of laser light source is 100 mW. Lin, Yingying, and Zhu (2014) and Du et al. (2016) presented their research result on a prototype of multispectral LiDAR with 32 bands. An APD array detector was used to convert the spectrally separated laser light to electrical signal. The multispectral LiDAR was validated at a rice field through placing in the front of the LiDAR away from 4.0 m. Sun et al. (2014) presented a laboratory-based prototype of the hyperspectral full waveform LiDAR with 32 wavelengths at a spectral range of 409 nm thru 914 nm. The LiDAR instrument was tested away from 7 m for monitoring the 3D structures of and the biochemical parameters of vegetation. A 32 element line PMT array detector was used to convert the spectrally separated laser light signals to electrical signals. Chen et al. (2018) designed a 17 channel HSL for ore classification.

(6) Chen et al. (2019)and Shao et al. (2019) reported, respectively, a prototype of spectral resolution hyperspectral LiDAR system at a spectral range of 500 nm to 1000 nm and spectral sampling interval of 10 nm or 5 nm which can achieve 51 or 91 spectral channels with time division multiplexing, but the HLS is not parallel measurement. It is use for coal/rock classification, vegetation red edge detection, angle effect of leaf reflectance, and assess its feasibility in agriculture application.

Although a few efforts have been made and a few advances have been achieved on multi/hyperspectral LiDAR study and development, the limits of these LiDAR instruments expose: (1) laboratory-based scientific experiment instruments without considering the airborne platform outdoor environment; (2) the most number of bands with 32 bands of parallel measurement; (3) usually the smallest spectral resolution with 20 nm, and (4) ground borne-based (i.e., NOT airborne-based) instrument with a limited distance, such as maximum 20 m. Since the applications of AIRBORNE-oriented hyperspectral LiDAR with supercontinuum spectral bands (e.g., 10 nm spectral interval) in geoscience, agriculture (Hu et al. 2020; Li et al. 2019; Jiang et al. 2019), forestry and other fields have played an irreplaceable roles relative to either traditional LiDAR point cloud data or passive hyperspectral imagery, such as 3D chemical composition (chlorophyll content), 3D physiological and biochemical parameters along vertical profiles of vegetation (Morsy, Shaker, and El-Rabbany 2017; Sun et al. 2017; Nevalainen et al. 2014; Schlemmer et al. 2013; Clevers and Gitelson 2013), this paper therefore presents the advances on airborne-based supercontinuum laser hyperspectral (SCLaHS) LiDAR with 50 bands covering 400 nm to 900 nm at a spectral resolution of 10 nm. This paper provides readers with a whole picture in the design of the SCLaHS LiDAR system and part of implementation in experiments.

3. Design of SCLaHS LiDAR system

The architecture of a SCLaHS LiDAR is depicted in Figure 1, which consists of four key parts below:

(1) Supercontinuum laser source with 50 bands covering from 400 nm to 900 nm at a 10 nm spectral interval,

(2) Large co-axis/co-aperture transceiver optical-mechanical subsystem,

(3) High spatial-spectral-temporal resolution full-waveform laser hyperspectral echoes rapid detection, and

(4) In-flight calibration and validation of the prototype of SCLaHS LiDAR onboard airborne.

3.1. Supercontinuum laser source with spectrum coverage at 400 nm to 900 nm

3.1.1. Pulse dynamics regulation and control of the picosecond fibre laser oscillation

In order to produce a supercontinuum laser source, picosecond fibre laser oscillator is used to provide seed source for the entire all-fibre picosecond laser system and the scheme is shown in Figure 2. The laser oscillator is essential for the picosecond laser system since the output of which entirely relies on the pulse quality, stability and other properties of the laser oscillator. For this reason, this RG 1 firstly design the laser cavity by solving the non-linear Schrödinger equation. By doing this, the dynamics of pulse evolution in the fibre picosecond seed source is resolved, and the output characteristics of the

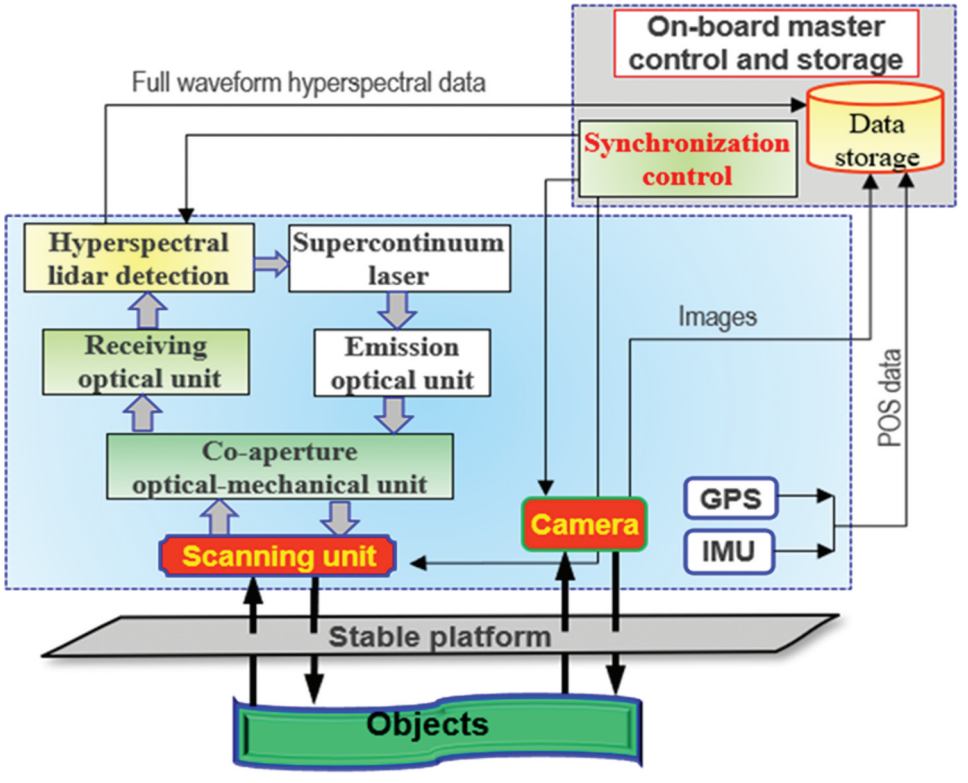

Figure 1. Architecture of a SCLaHS LiDAR.

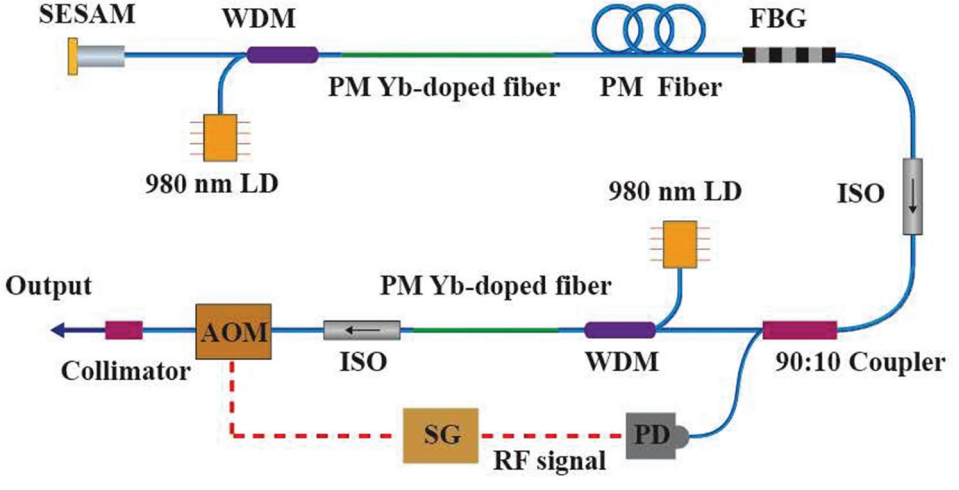

Figure 2. Supercontinuum laser seed source through fibre picosecond laser oscillator. SESAM: semiconductor saturable absorber; FBG: fibre Bragg grating; ISO: isolator; WDM: wavelength division multiplexer; AOM: acoustic optical modulator; SG: signal generator; PD: photo detector.

parameters, such as power, pulse width, time jitter, power stability, etc., are evaluated. Accordingly, other parameters such as fibre length, filter bandwidth, and SESAM (semiconductor saturable absorber mirrors) modulation depth in the laser seed source are determined. Moreover, a noise source is introduced into the simulation model to explore the dynamics of nonlinear coupling of various noise sources in the resonant cavity. Based on the results of numerical simulation, proper design of the laser factors, such as nonlinearity, dispersion, and dissipation of the adjustable picosecond laser seed source, results in a non-linear attractor, which largely suppresses the amplification of quantum noise, effectively improves the stability of the laser, and increases the signal-to-noise (SN) ratio of laser seed source.

3.1.2. Optimal design of high-power picosecond laser amplifier and pulse picker

The design for the high-power picosecond laser amplifier system is shown in Figure 2. To meet the requirement of high-average power and energy for the input pulse of the main amplifier, this research designs a pulse preamplification system for the picosecond laser oscillator. The main function of the preamplifier is to amplify the laser output average power with high signal-to-noise ratio, meanwhile, a high pulse quality and high beam quality during amplification process is maintained. Because core doped active fibre with a large diameter can effectively increase the single-mode area, and high doping concentration can shorten the fibre length and reduce the nonlinear accumulation effect, this paper establishes mathematical model for simulation of the pre-amplification system on the basis of the actual dynamics of pulse propagation in the gain fibre by solving nonlinear Schrödinger equation. In combination with experiments, the core diameter, length, and doping concentration of the fibre in the pre-amplification are optimized in order to effectively reduce pulse distortion and spectrum modulation caused by nonlinear effects and overcomes the drift of the centre wavelength to the long wave direction caused by stimulated Raman scattering.

In addition, to meet the requirement of high-energy picosecond laser system, this paper proposes using a pulse picker to discretely adjust the repetition rate of the laser system between 20 kHz to 10 MHz. The proposed pulse picker is performed by using an acousto-optic modulator (AOM) with polarization-maintaining fibre pigtails. Considering the high insertion loss of the acousto-optic modulator, a two-stage amplifier is designed. The acousto-optic modulator is located between the two-stage amplifiers, as shown in Figure 3.

3.1.3. Optimal design of multicore nonlinear photonic crystal fibre

The output power of a single nonlinear optical fibre is limited by the core size. Moreover, the expansion of the nonlinear spectrum is usually happened at the long waves under the

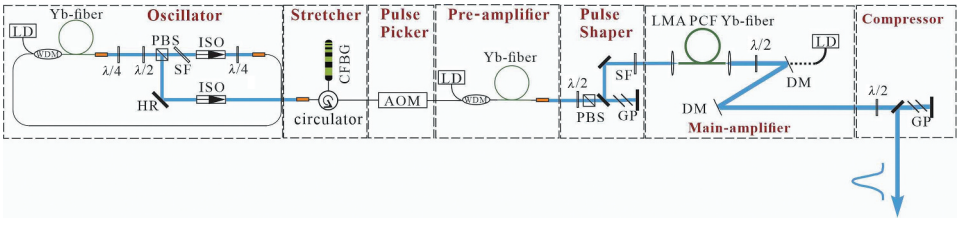

Figure 3. High power picosecond fibre chirped pulse amplification system.

pump of picosecond laser within 1 m band. These factors largely limit the generation of spectrum ranging from 400 nm to 900 nm and lead to low efficiency of super-continuum conversion. As a result, it is difficult to generate a high-power super-continuum laser light source covering 400 nm to 900 nm. For this reason, this paper proposed a novel method, which uses a highly nonlinear fibre with special dispersion curve and zero dispersion wavelength.

Both the computer simulation and the experimental verification of the nonlinear pulse propagation dynamics will simultaneously be used to solve the problem of low efficiency of super-continuum generation in the visible band. Furthermore, the visible band is extended to achieve 400 nm to 900 nm. To this end, a high-nonlinearity optical fibre with a multi-core structure is selected and investigated (see Figure 4). A study on manipulating the nonlinear process that impacts the evolution of the in-phase super mode generation is conducted. The investigated results are finally used for implementation of a high-power supercontinuum laser with the in-phase super mode generation. Figure 5 is the final experimental results.

3.1.4. Optical-mechanical-electrical integration for high-power supercontinuum laser

To the end of a high-power supercontinuum laser source covering band of 400 nm to 900 nm long-term stable operation, the optical-mechanical-electric integration is proposed. The major steps include

Step 1: This paper first proposes an entire super-continuum laser source consisting of several submodular, such as the oscillator, preamplifier, pulse picker, and laser pump, which are independently investigated, and manufactured to facilitate the replacement and maintenance. The picosecond laser seed source is independently controlled using a consistent temperature at approximately 25°. In accordance with the requirement of isolating the vibration, a support structure is designed to guarantee the long-term stability operation. A user-friendly interactive panel interface is also designed to make

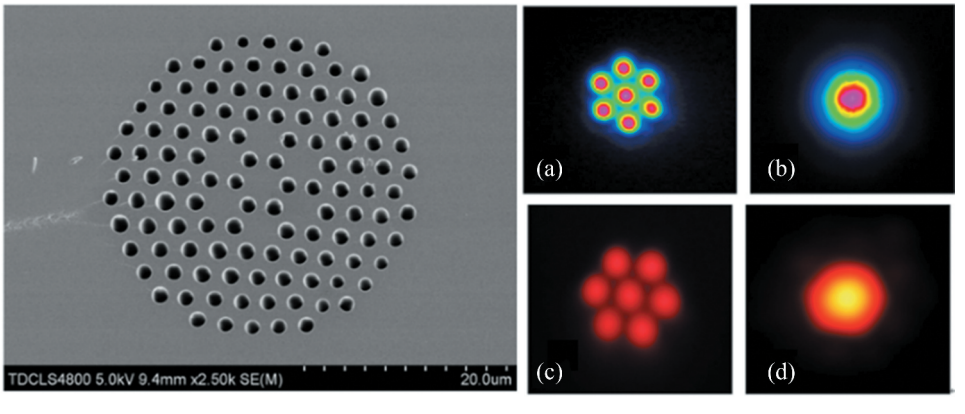

Figure 4. A highly nonlinear photonic crystal fibre end with seven-core structure and its output beam distributions at near- and far-observations. (*a*) Measured near field beam distribution with beam profiler; (*b*) Measured far field beam distribution with beam profiler; (*c*) Photo of near field beam distribution; (*d*) Photo of far field beam distribution.

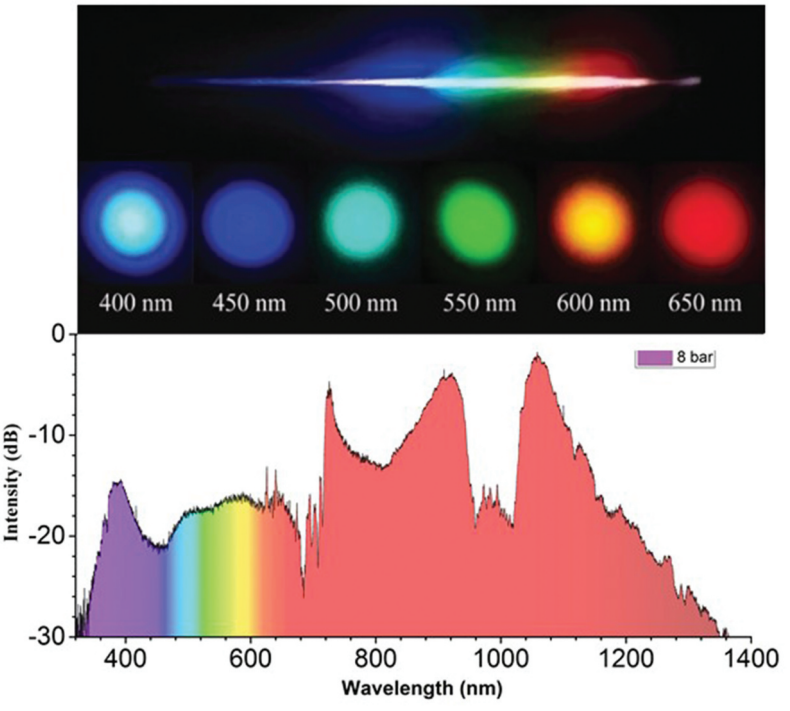

Figure 5. Experimental result of high-power supercontinuum laser at 400 nm to 900 nm.

users easy to start up laser, setup the parameters, such as repetition frequency, and alarming of laser operation stability.

Step 2: This paper proposes selecting a high light-transmittance adhesive, which much matches the refractive index of the fibre ceramic ferrule, to tightly bond SESAM and fibre ceramic ferrule. This type of high light-transmittance adhesive can effectively reduce the interface reflection at the bonding interface without losing laser energy. Therefore, the SESAM and polarization-maintaining (PM) fibre cables can be effectively merged.

Step 3: This paper presents a low-loss welding method used specifically for polarization - maintaining (PM) fibres with different sizes of core diameters and an optimal fibre taper method: The two types of methods can (1) enhance the quality of mode matching to avoid the degradation of transmitted laser quality, and to avoid the depolarization of transmission pulses; (2) reduce the spurious echo at the spliced point to avoid crosstalk to the mode-locking stability of the oscillator; (3) rationally optimize the active and passive heat conduction structures of the welding point to increase the maximum optical power at the spliced point and to avoid effectively laser beam distortion caused by the thermal lens effect.

Finally, a prototype of supercontinuum laser light source covering a spectral range of 400 nm to 900 nm at a spectral resolution of 10 nm is generated (see Figure 6). The characteristics of the laser light includes pulse width < 2 ns, average power > 5 w, the repetition frequency at 20 kHz to 10 MHz, continuous working time for 4000 hours; optical spectrum coverage at 400 nm to 900 nm, average optical spectral power density > 15 mW nm^{-1}.

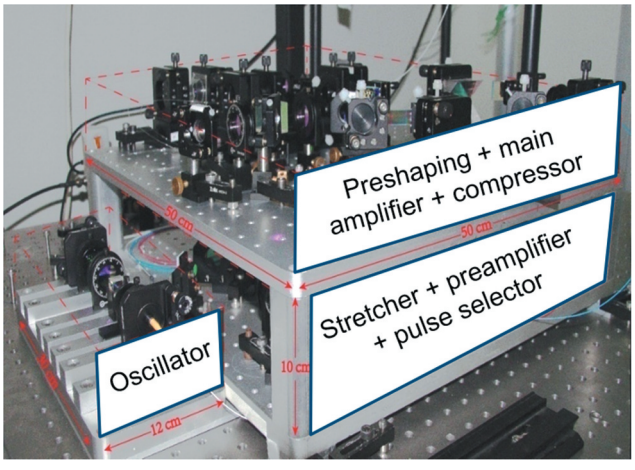

Figure 6. Optical-mechanical-electrical integration for high-power fibre laser and supercontinuum generation system.

3.2. Large co-aperture optical-mechanical subsystem

3.2.1. Large co-aperture transceiver optical subsystem

The laser emission system is designed to implement the collimation and expansion of the output beam, to reduce the divergence angle of the beam, and to enhance the radiation intensity of the far-field laser beam. Especially, the designed large co-aperture laser receiving system is used to detect the weak signals returned from the ground objects.

The subsystem uses a double-sided (back-to-back) mirror pendulum scanning system to achieve a more than 30° field of view (FOV) observation. The full waveform synchronous detection of the echo signal is implemented through the co-axis/co-aperture of the laser transmitter and receiving optical subsystem as well as the echo detection subsystem (Figure 7).

The large aperture transceiver optical system carries out the synchronous observation and detection of 50 bands laser hyperspectral echo signals. The laser hyperspectral emitting uses a back-to-back mirror to scan an entire cycle as a period. The cross-flight direction scanning combines the moving platform to achieve strip-by-strip observation in parallel mode. The parallel strip data has no overlap. The high-precision aperture of the transceiver optical subsystem is designed with a vertical optical axis. A 45° folding mirror is placed on the optical path to make the transmitter and transceiver optical axis parallel. Through precise adjustment of a reasonable aperture ratio of the folding mirror and the transceiver optical system, an optical system with higher than 0.2 mrad co-registration accuracy is reached, as shown in Figure 7.

Since the imaging spectral range is specified at 400 nm to 900 nm with the requirement of colour aberration-free, the optical subsystem of laser transceiver is proposed to adopt a reflective optical system structure. To meet the requirements of large aperture, meanwhile miniaturization of the instrument size, an off-axis two-mirror high-order aspheric surface system structure is proposed, and F # with 1.5 in the optical system is designed and implemented. In addition, according to the relationship of the relative aperture square inversely proportional to the detection energy, the signal-to-noise ratio

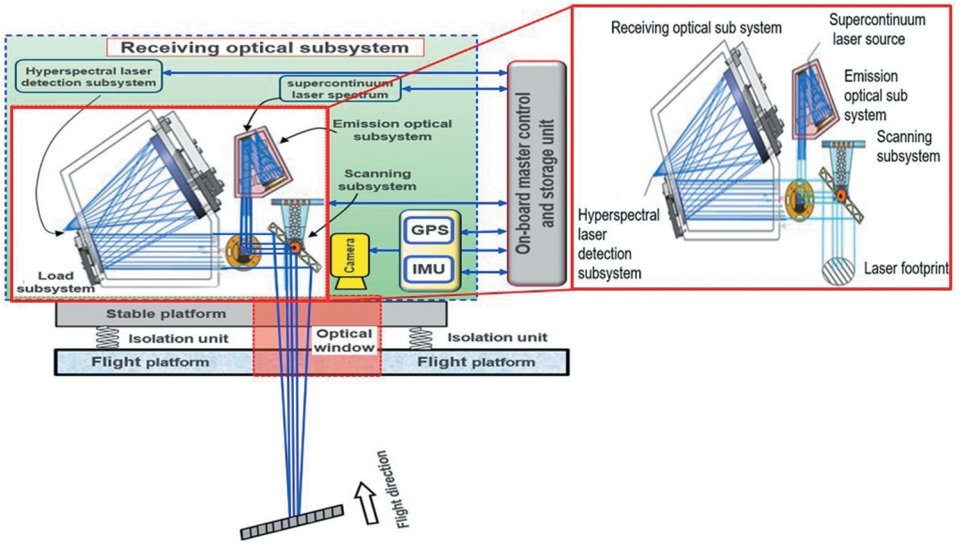

Figure 7. Co-axis/co-aperture transceiver optical-mechanical system.

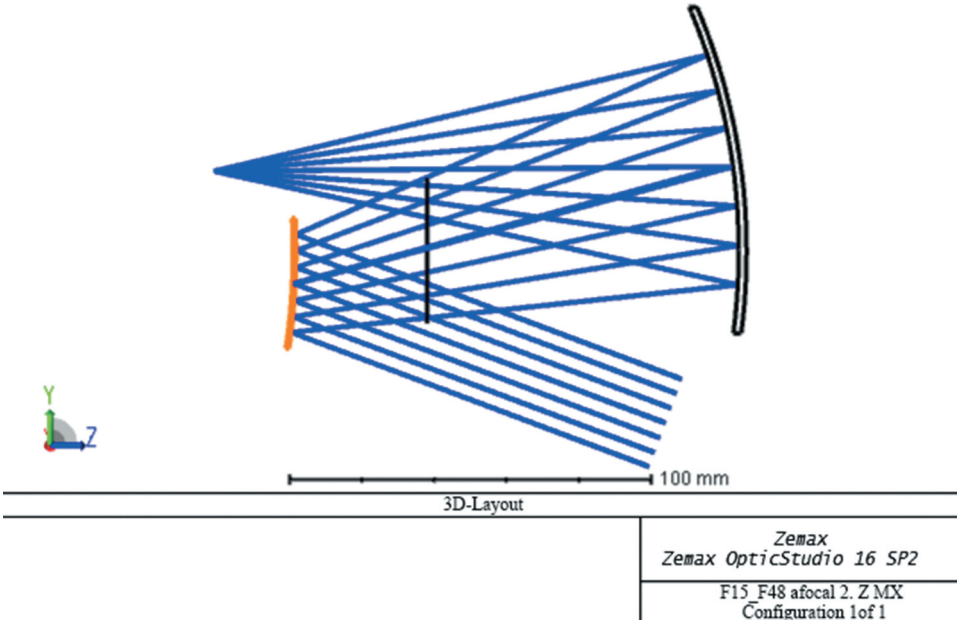

Figure 8. Design of the emission optical subsystem.

(SNR) of the entire system can thereby be greatly improved. The position of diaphragm is optimized to achieve an optimal relationship between the configuration of the image side image telecentric and the optical connection. With the design above, the focal length of the transmitting optical system is 62.5 mm, and the aperture diameter is 30 mm, and the laser point interval is less than 1mrad. The designed result is shown in Figure 8.

In addition, the receiving optical subsystem is designed as follows. Microcrystalline materials with low linear expansion, which has a good stability under various environments, is used as the mirror embryo. The 5 axis CNC (computer numerical control) milling, magnetorheological polishing, ion beam shaping and other manufacture techniques are used to manufacture the off-axis aspheric surface telescopes. With the design above, the focal length of the receiving optical system is 150 mm and the aperture is 100 mm. The details of relationship between range and FOV can be referenced to the Zhou et al. (2015). The modulation transfer function (MTF) > 0.8 (@ 16.7 l p mm^{-1}) can be achieved (Figure 9).

In order to manufacture the convex hyperboloid, which is one of the most primary mirror in this subsystem, back sphere zero compensation calibration and auto-collimation method are used to detect whether the optical path is interference. For the secondary mirror, which is the conic aspheric mirrors, the zero-compensation method is used to calibrate and compensate the accuracy of the mirror shape. The optimal convergence algorithm based on aberration compensation is applied in the installation of quantitative automatic system with fixed degrees of freedom. The entire installation structure of the receiving optical subsystem is shown in Figure 7.

3.2.2. Double-side mirror scanning system

The SCLaHS LiDAR is designed to use a rotating point scanning mode to collect point cloud data. The FOV is designated at 30°, and the scanning resolution is better than 1 mrad, which is controlled through a scanning control unit. The rotation speed of the scanning mirror is related to the flight direction of the airborne platform, in order to

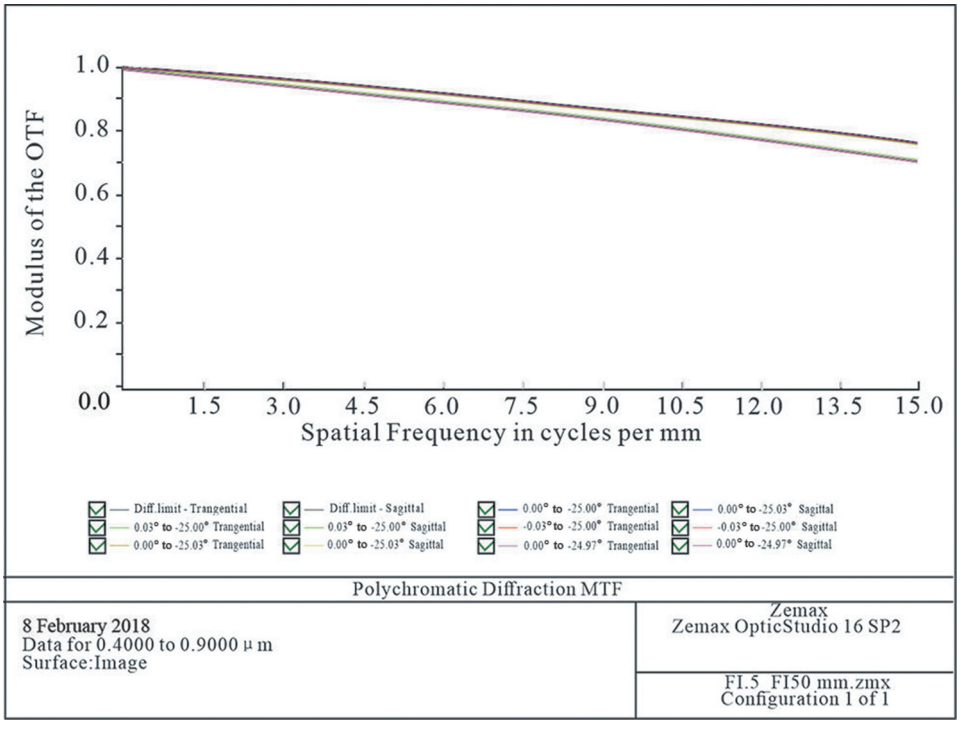

Figure 9. The MTF result of the telescope.

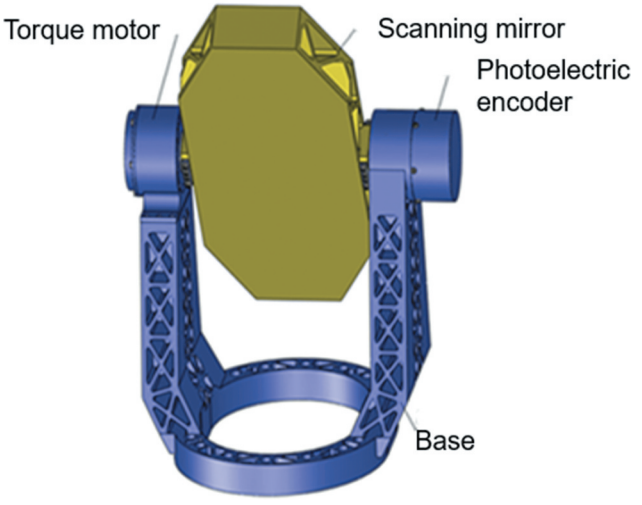

Figure 10. The 3D drawing of the scanning mirror subsystem.

ensure to collect a uniform distribution of 3D point cloud data. The effects of the scanning angle can be referenced to the Qin et al. (2017a and 2017b).

The SCLaHS LiDAR scanning subsystem consists of double-sided mirror, driving motor, rotational shaft, photoelectric encoder, base, and control unit, etc. which are shown in Figure 10. The scanning mirror is designed with a double-sided symmetrical structure, which has a good stationary balance. Beryllium aluminium alloy is used to reduce the inertia moment of the mirror body, and increase the rigidity of the mirror body. The surface of the mirror body is designed as a triangle. The ratio of the diameter-to-thickness is 8:1. The surface of the mirror body is painted and polished using nickel. Finally, a double-sided mirror with an aperture of 180 mm and a surface accuracy of better than 1/30 λ (λ = 632.8 nm) is implemented. This scanning subsystem designed in this paper ensures a high-stability of scanning and a high-quality of mirror surface shape.

A torque motor is used to drive the scanning subsystem, which is closed-loop controlled by a high-precision 16-bit absolute photoelectric encoder. A10 kHz high-frequency readout is used to coordinate the calculation and the closed-loop feedback control of 3D point cloud data. In accordance with the entire system's requirements for positioning accuracy, fast tracking ability, and scanning speed stability, the three closed-loop proportional-integral-derivative (PID) control methods, including the outer ring, positioning ring, speed ring, and inner current ring, are adopted. The experimented tests demonstrated that the uniform speed of the pointing mirror has been achieved the accuracy of over approximately 1% rotational fluctuation.

3.3. High-resolution full-waveform laser hyperspectral echo rapid detection

3.3.1. Holographic concave grating for hyperspectral imaging

Due to very weak laser hyperspectral echoes during imaging at day and night, as well as a moving platform, this paper presents miniaturizing the aberration correction holographic concave grating spectroscopy to generate hyperspectral spectrometry at real-

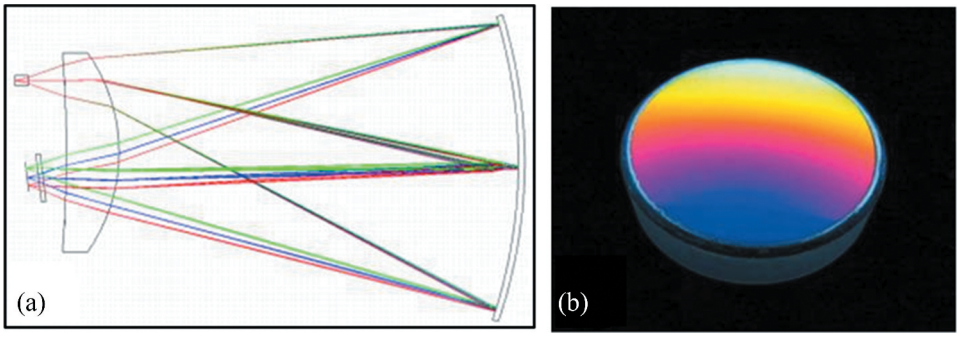

Figure 11. Holographic concave grating spectroscopic design (*a*) and implementation (*b*).

time. To this end, one of the most important units is the holographic concave grating spectroscopic (see Figure 11). With considering the large aperture, wide spectral band covering 400 nm to 900 nm, and high spectral resolution at 10 nm, this paper integrates both the correction lens and aberration correction holographic concave grating. A compact grating dispersion spectroscopic structure is designed through decentring and off-axis method. In addition, the fibres-coupled method is proposed for effective data transmission to ensure that incident light can be efficiently transmitted to the pinholes slit through the fibre (see Figure 12).

Due to the adoption of large aperture design, it can be imagined that the lens aberration is significant. For this reason, this paper presents the spectral line bending and colour distortion of prism correction to correct lens aberrations. This design can effectively ensure imaging quality within the spectral range. Meanwhile, the holographic grating stray light remains low, which can effectively control stray light. Under the condition of meeting the signal-to-noise ratio of the spectrum requirement, the diffractive order and the reticle density of the grating are optimized, and the high diffraction efficiency in the range of the working band is obtained by using the blazing method. With the design above, the spectral resolution can meet the requirements at 10 nm interval. Moreover, a miniaturization and compact hyperspectral imaging subsystem can be reached through optimizing the optical mirror spacing and the apex curvature radius of each mirror.

3.3.2. Rapid detection of full-waveform laser hyperspectral echoes

Because of extremely high spectral resolution of 10 nm with 50 bands and high-spatial sampling resolution of 2 mm, it is a very challenging task to implement the real-time detection of laser hyperspectral echoes. For this reason, this paper presents application of the streak camera, whose basic working processes are as follow (see Figure 13).

(1) A linear slit is set up in the front of the photocathode of the detector, which is equivalent to a linear detector. The direction of the slit is the same as the spectral intensity distribution of the grating does. When laser light pulse signals with different distributions in space, time and intensity pass through the slit and the incident optical system, and then are imaged, finally arrive at the photocathode. Afterwards, the light pulse signal acts with the photocathode each other to generate electrons. Since the time of reaching detector for each of echo signals at different distances (from the different target) is different, the

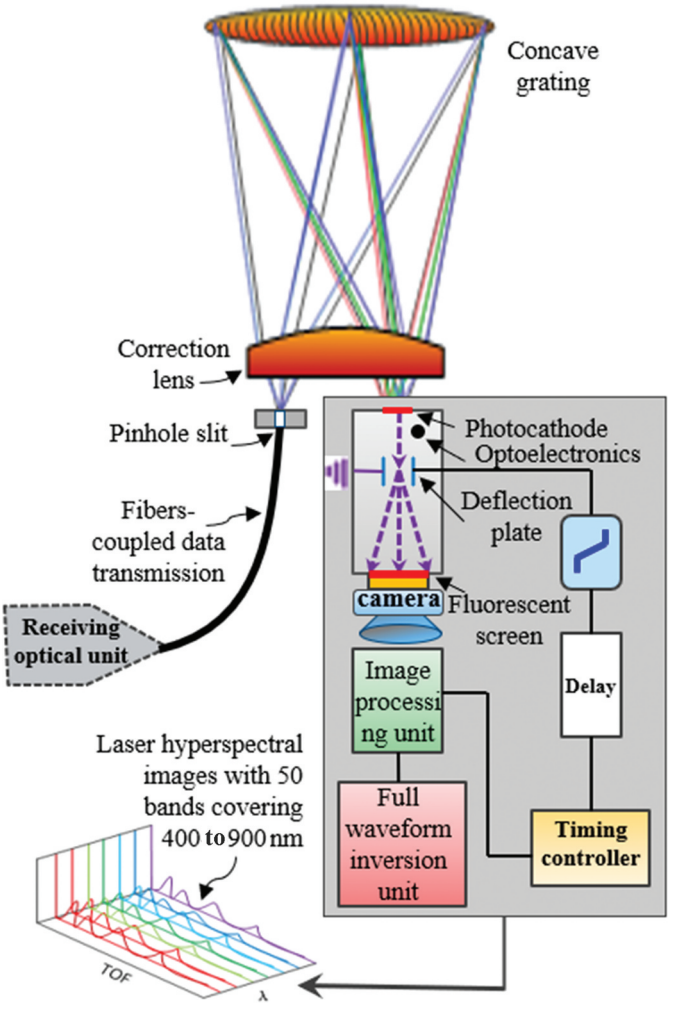

Figure 12. Hyperspectral imaging principle subsystem, which consists of fibres-coupled, narrow slit, miniaturized aberration correction lens, holographic concave grating, photocathode, deflection plate, fluorescent screen, camera, image processing, full-waveform retrieval, delayer, timing controller, etc.

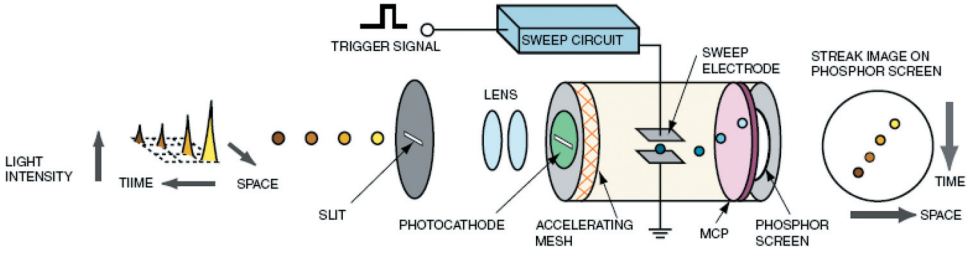

Figure 13. Working processing of a streak tube (Courtesy of Hamamatsu for Guide to Streak Cameras, https://www.hamamatsu.com/resources/pdf/sys/SHSS0006E_STREAK.pdf).

photocathode has different scanning voltages when passing through the deflection system. As a result, linear stripes are generated in the direction perpendicular to the slit. Therefore, a series of linear stripe images are generated in the direction of the slit, which is called line array imaging.

(2) The electron pulse passes through a pair of deflectors, and a fast scanning bias voltage is acted on the deflector. The electrons, which pass through the deflector at different times, are deflected to different positions in space. The laser hyperspectral echo signals at 50 bands covering 400 nm to 900 nm at a spectral resolution of 10 nm are reflected by the ground target, and are converted into electrical signal by streak tube.

(3) The electrons deflected are multiplied and amplified when they pass through the microchannel plate, then bombard the fluorescent screen to generate light signal.

(4) The light pulses at different temporal times are ordered on the fluorescent screen from top to bottom. The vertical direction on the fluorescent screen represents the time information of the pulse, the brightness of the signal represents the intensity of the pulse, and the horizontal direction represents the horizontal position of the pulse. The echo signals of the target at different distance correspond to the linear stripes at different positions on the fluorescent screen (see Figure 14).

(5) Through the inner scanning module in the detector, the laser pulse sequence signals are converted into image information spatially arranged along the scanning direction. With the characteristics of the correlation between spatial position and scanning speed, the time information can be calculated. Through large-slope linear scanning technology, high-temporal resolution detection with high stability are generated. It can be estimated that the temporal-resolution accuracy can reach better than 10 ps, which meets the mm-level distance accuracy requirements.

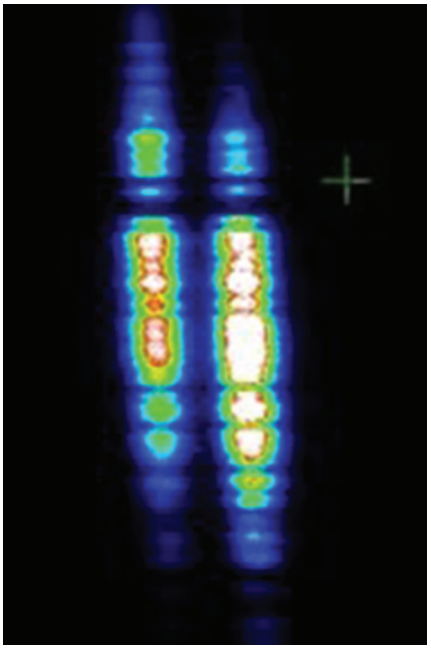

Figure 14. The initial experiment result using streak camera.

The key techniques for real-time detection of the hypercontinuum laser hyperspectral echoes from ground objects are:

(1) Single-photon weak signal detection: A micro-channel board is used to detect the single-photon weak signal. The micro-channel board is composed of millions of electron multiplier tubes, and each electron multiplier tube is coated with secondary electron emission material with a gain of up to 107, and can detect single electron. When the microchannel plate is placed inside the detector, each of electron is multiplied, which can detect extremely weak light signals (see Figure 15).

(2) Large spectral range detection: while increasing the input light energy threshold, the light noise level will have to be reduced as much as possible. For this reason, high-sensitivity photocathode, ultra-high vacuum transfer cathode and low-noise microchannel board can achieve better than 10,000: 1 dynamic range.

(3) Solar light deflection: In order to avoid to receive sunlight components and increase the detection signal-to-noise ratio, a natural light sampling gate is set in each detection channel, and the natural light noise is removed by an algorithm during the signal processing. The details of algorithm can be referenced to Zhou and Zhou (2018).

(4) 3D image recording: On the fluorescent screen, the transverse direction represents the wavelength information, and the longitudinal position corresponds to different distances. The ground target is three-dimensionally imaged by LiDAR scanning operation. With the application of streak tube, the time resolution of streak tube can reach 10 picoseconds, which corresponds to the distance accuracy of approximately 1.5 mm. Full-waveform laser echo inversion method: The laser echo is split using the grating 50 beams from 400 nm to 900 nm to form 50 channel detection. Each channel forms a laser pulse image. The inversion generates a full-wave length laser pulse sequence in the time domain, combined with the hyperspectral. The information generates point-by-point hyperspectral full-waveform point cloud data with record of 12 bits (Figure 16). The details of similar experimental test can be referenced to the Zhou et al. (2015) and Hu et al. (2017).

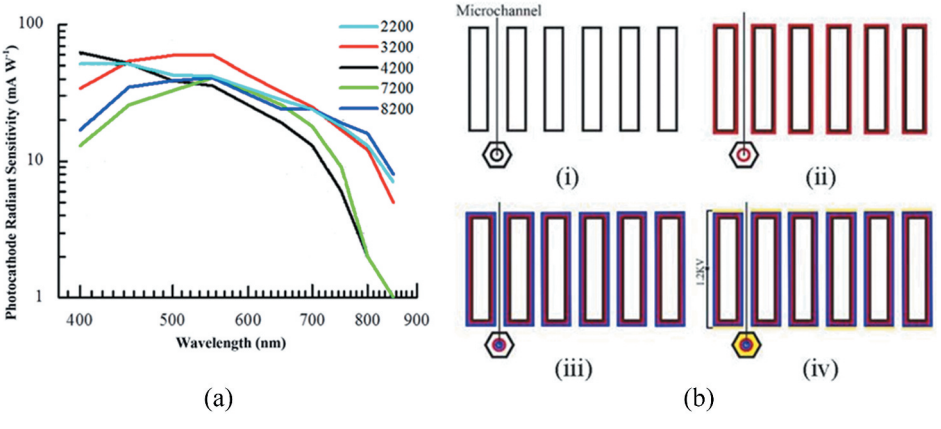

Figure 15. (*a*) Ultra-high sensitivity photocathode preparation technology, and (*b*) high-gain low-noise multiplication layer deposition technology at(i)Non-coating, (ii)resistance coating, (iii) emission coating, and (iv)conductive coating.

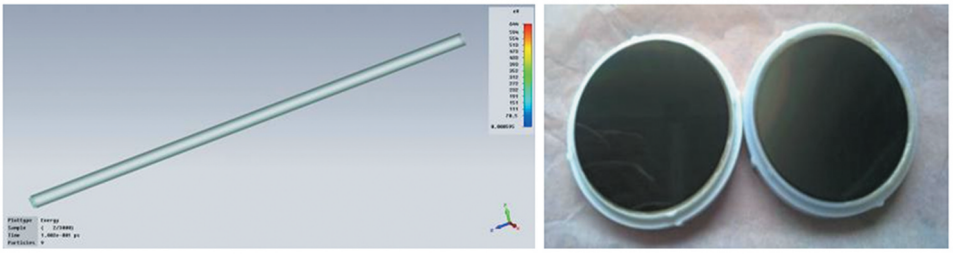

Figure 16. (*a*) Microchannel board gain simulation, and (*b*) micro channel plate photo.

With such an innovative development in use of the array electron multiplier detector and the miniaturized, high-resolution holographic grating spectroscopic, a large field of view, high frame rate, high spatial/temporal resolution, and long-range detection capabilities can be achieved.

3.4. Assembly for the prototype of SCLaHS LiDAR

3.4.1. Multi-sensors synchronous control and reference datum

The Global Positioning System (GPS) in the SCLaHS LiDAR contains a high-frequency clock, which is controlled through the central control unit. The generated high-frequency clock is used as the reference datum of the entire system of SCLaHS LiDAR. The entire system is cooperatively operated through synchronous trigger control circuit. The working sequence of multiple sensors is shown in Figure 17.

In addition, this paper uses the high-frequency of frame CCD camera-assisted image geometric correction to improve the efficiency of airborne observation data. To minimize the time-domain dispersion effect of the received radiation caused by the flutter of the load system, vibration isolation unit with passive low-pass filtering and stabilization platform with active boresight stabilization are combined to control the stabilization of entire observation (Figure 18).

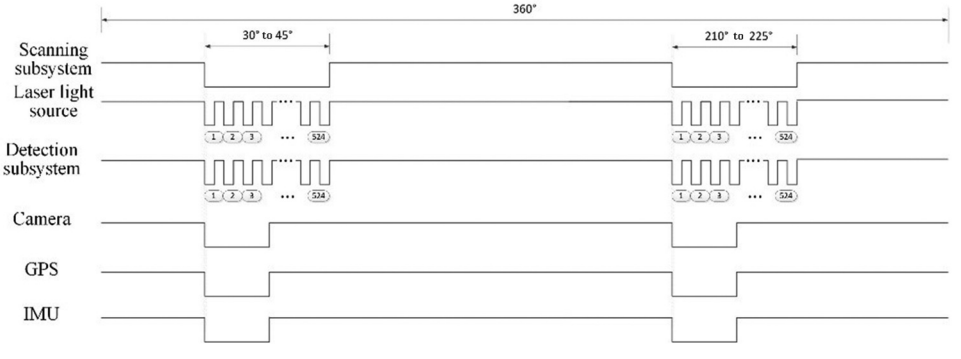

Figure 17. Timing series of multi-sensor operation.

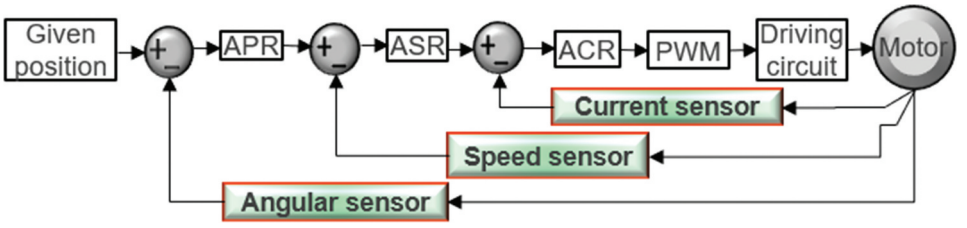

Figure 18. System control scheme block diagram.

3.4.2. Assembly for the prototype of SCLaHS LiDAR

A prototype of SCLaHS LiDAR consists of several modules. An effective integration of each module on a stable and reliable platform into a compact, lightweight and high structural rigidity is important. For this reason, the transceiver sub-system uses the flexible and bendable optical fibres to couple the laser and the detection sub-system to achieve a high compactness and flexible module. In addition, the laser light source is also compacted in a lightweight small module. Finally, a prototype of SCLaHS LiDAR can be assembled (see Figure 19), which can reach the following specifications.

(1) The optical specification of the prototype AHL:
Spectral range: 400 nm to 900 nm,
The spectral resolution: ≥ 10 nm,
Number of bands: ≥ 50,
Frame rate: ≥ 200 fps,
The number of quantization for laser full waveform echo: 12 bits,
F # = 1.5, and
MTF > 0.7.

(2) The geometric specification of the prototype AHL:
Detection distance: ≥ 500 m,

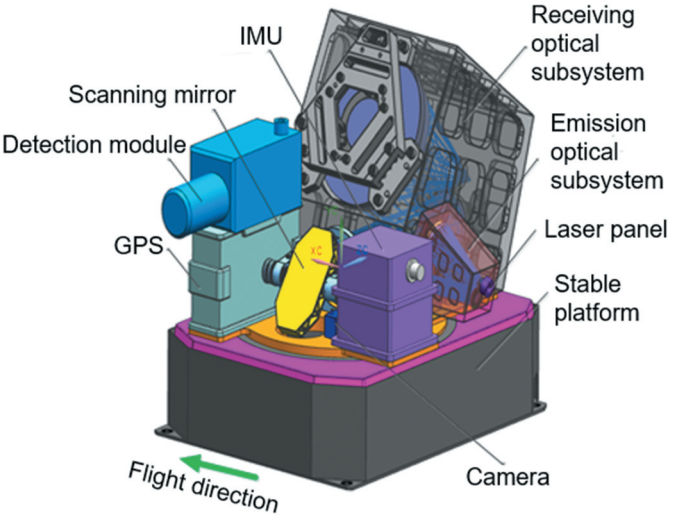

Figure 19. The 3D layout of the SCLaHS LiDAR.

Field of view: ≥ 30°,
The size of the laser footprint: ≤ 0.1 mrad,
The laser dot spacing: ≤ 1mrad,
Ranging resolution: ≤ millimetre level,
Co-registration accuracy of transmitting-receiving: ≤ 1/5 pixel, and
The Line of Sight (LOS) stabilization accuracy: ≤ 0.1 mrad.

(3) The picosecond laser seed source specification of the prototype AHL:
The pulse width: ≤ 2 ns,
Average output: > 5 W,
Repetition frequency: 20 kHz to 10 MHz,
Continuous operation period: 4,000 hours, and
The average spectral power density at the 400 nm to 900 nm: ≥ 15 mW nm^{-1}.

3.4.3. In-flight airborne geometric and radiation Calibrations

To evaluate the technical parameters of, and verify the reliability and accuracy of the SCLaHS LiDAR prototype's system, airborne-based in-flight calibration and application demonstration intends to be conducted. A test field located in Songshan, Henan Provience, China is proposed as a candidate of the field experiments. Airborne platforms (airplane or helicopter) are used to carry out the in-flight calibration. Meanwhile, the corresponding actual ground observation data are obtained and are provide by the Songshan, Henan Province, China. The major work include as follows:

(1) Geometrical calibration of the SCLaHS LiDAR: Airborne-based in-flight calibration and verification is proposed for at least 3 times in total, in which 2 times should be deployed at daytime and 1 time at night-time. Geometrical calibration techniques based on geometric error sources and error propagation law are developed. A high-accuracy of model for system error correction is developed. Geometrical calibration model, including IMU off-angle and the GPS offset measurement is developed to solve the unknown parameters (see Figure 20).

(2) Radiation calibration method: The active hyperspectral radiation calibration model based on atmospheric characteristics, target scattering characteristics, incident angle and distance and other factors is developed. Meanwhile, the attenuation of a few factors such as transmission distance, incident angle, and emission energy difference, and the influence of a few factors, such as solar radiation measurement, typical target surface reflectance measurement will be considered for the radiation calibration of the SCLaHS LiDAR (see Figure 20).

(3) Development of algorithm theoretical basis: Algorithm theoretical base for the full-waveform laser hyperspectral echo rapid detection and the point cloud data processing will be developed. Application demonstration on SCLaHS LiDAR's unique role in forest physiological and biochemical parameters along its vertical layered profile during the day-night alternation will also be developed (see Figure 21). The details can be referenced to the Qin et al. (2018) and Luo et al. (2019).

4. Conclusions

This paper presents innovative techniques in development of a prototype of the LSLaHS LiDAR. The major breakthroughs are as follows.

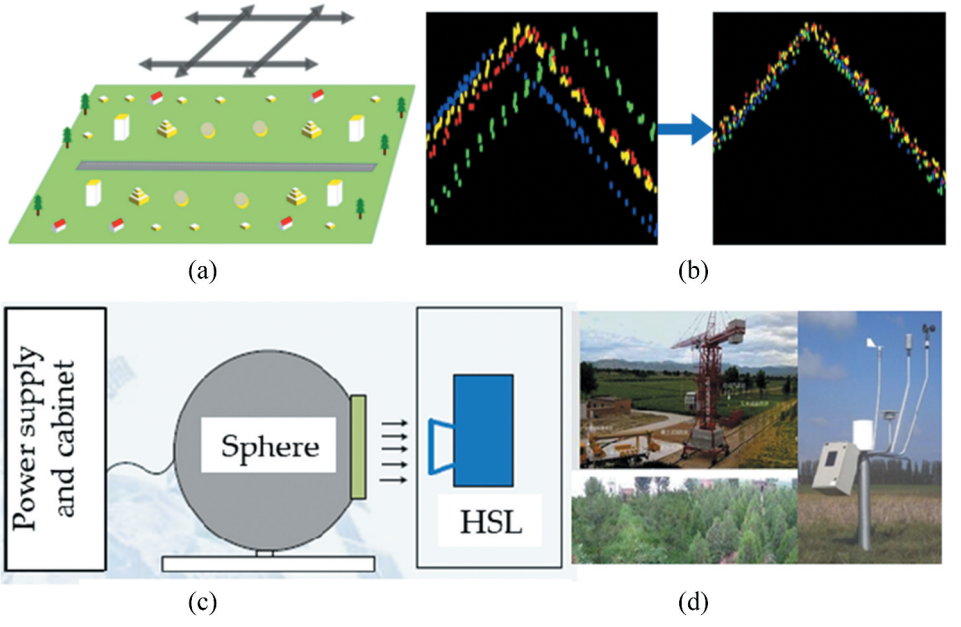

Figure 20. In-flight airborne calibration of the SCLaHS LiDAR, (*a*) Calibrator settings, (*b*) Calibration effect diagram, (*c*) Laboratory radiation calibration, and(*d*) Calibration field.

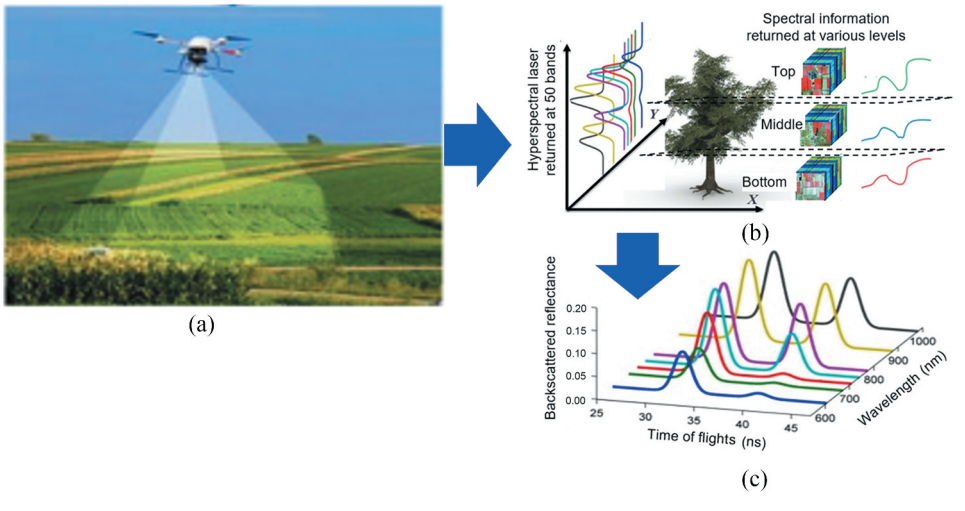

Figure 21. a) Application demonstration for SCLaHS onboard airborne, (b) typical application demonstration of the SCLaHS LiDAR at multiple spectral imaging, (c)fitted backscattered reflectance waveforms (Courtesy of the full waveform of LiDAR is from Hakala et al. 2012).

(1) Supercontinuum spectral coherent beam combination using multi-core microstructure fibre: In order to provide a 400 nm to 900 nm supercontinuum laser source at 10 nm spectral resolution, an all-polarization maintaining fibre and an ultra-long cavity structure are utilized to generate the high-power narrow-pulse laser. It can not only generate laser

spectrum at 400 nm to 900 nm efficiently, but also ensure high-power laser pulses output through combing the multi-core structure and the highly nonlinear photonic crystal structure generated by the enhancing visible light band. These innovations include physical mechanisms related to nonlinear dynamics, ultra-narrow pulse laser design, and the optimization of nonlinear photonic crystal fibre structures makes the SCLaHS LiDAR compacted.

(2) The SCLaHS imaging at a high temporal resolution: a miniaturized aberration correction holographic concave grating spectroscopic is presented for a large dynamic range spectral detection, and streak tube technique is used for 50 bands laser echoes detection at high spectral-spatial-temporal resolution and dynamic airborne platform to reduce detection errors caused by such as geometric aberrations (e.g., lens curvature, astigmatism), and time dispersion. To meet the fast detection of the returned SCLaHS signals at a high-temporal resolution, this paper presented high-accuracy, large-slope, high-linear scanning technique. To detect very weak signal returned from the ground objects, this paper presented electronic multiplication method through microchannel plates.

In a word, the innovative contributions from this paper consists of (1) investigating the hypercontinuum laser hyperspectral RTM, including its spatial and spectral synchronous imaging; (2) developing the supercontinuum laser sources covering 400 nm to 900 nm at a spectral resolution of 10 nm; (3) developing large co-aperture optical-mechanical system for full-wave synchronous observation; (4) rapidly detecting full-waveform laser hyperspectral echoes at very high spectral-spatial-temporal resolutions.

Author Contributions

G. Zhou proposed the idea, wrote the whole manuscript, conceived and designed the experiments, and finalized the manuscript; X. Zhou collected the material and wrote initial versions of Introduction; Y. Song conducted the part of experiments and revised partial illustrations, Other authors wrote the Chinese version and participated in discussion and analysis. All authors have read and agreed to publish the version of this manuscript.

Disclosure statement

The authors declare no conflict of interest.

Funding

This paper is financially supported by the National Natural Science of China (the grant #: 41961065), Guangxi Science and Technology Base and Talent Project (the grant #: Guike AD19254002); the Guangxi Innovative Development Grand Program (the grant #: GuikeAA18118038 and GuikeAA18242048); Guangxi Natural Science Foundation for Innovation Research Team (the grant #: 2019GXNSFGA245001), Guilin Research and Development Plan Program (the grant #: 20190210-2), and the BaGuiScholars program of Guangxi.

References

Chen, Y., J. Changhui, H. Juha, Q. Shi, W. Zhen, T. Mi, L. Wei, et al. 2018. "Feasibility Study of Ore Classification Using Active Hyperspectral LiDAR." *IEEE Geoscience and Remote Sensing Letters* 15 (11): 1785–1789. doi:10.1109/LGRS.2018.2854358.

Chen, Y., W. Li, J. Hyyppä, N. Wang, C. Jiang, F. Meng, L. Tang, E. Puttonen, and C. Li. 2019. "A 10-nm Spectral Resolution Hyperspectral LiDAR System Based on an Acousto-optic Tunable Filter." *Sensors* 19 (7): 1620. doi:10.3390/s19071620.

Chen, Y., E. Räikkönen, S. Kaasalainen, J. Suomalainen, T. Hakala, J. Hyyppä, and R. Chen. 2010. "Two-channel Hyperspectral LiDAR with a Supercontinuum Laser Source." *Sensors* 10 (7): 7057–7066. doi:10.3390/s100707057.

Clevers, J. G., and A. A. Gitelson. 2013. "Remote Estimation of Crop and Grass Chlorophyll and Nitrogen Content Using Red-edge Bands on Sentinel-2 And-3." *International Journal of Applied Earth Observation and Geoinformation* 23: 344–351. doi:10.1016/j.jag.2012.10.008.

Douglas, E. S., A. Strahler, J. Martel, T. Cook, C. Mendillo, R. Marshall, S. Chakrabarti, C. Schaaf, C. Woodcock, and Z. Li. 2012. "DWEL: A Dual-wavelength Echidna Lidar for Ground-based Forest Scanning." Paper presented at the 2012 IEEE International Geoscience and Remote Sensing Symposium (IEEE, 2012), July 22-27, Munich, Germany.

Du, L., W. Gong, S. Shi, J. Yang, J. Sun, B. Zhu, and S. Song. 2016. "Estimation of Rice Leaf Nitrogen Contents Based on Hyperspectral LIDAR." *International Journal of Applied Earth Observation and Geoinformation* 44: 136–143. doi:10.1016/j.jag.2015.08.008.

Gaulton, R., F. Danson, F. Ramirez, and O. Gunawan. 2013. "The Potential of Dual-wavelength Laser Scanning for Estimating Vegetation Moisture Content." *Remote Sensing of Environment* 132: 32–39. doi:10.1016/j.rse.2013.01.001.

Guerrero-Rascado, J., B. Ruiz, and L. Alados-Arboledas. 2008. "Multi-spectral Lidar Characterization of the Vertical Structure of Saharan Dust Aerosol over Southern Spain." *Atmospheric Environment* 42 (11): 2668–2681. doi:10.1016/j.atmosenv.2007.12.062.

Hakala, T., J. Suomalainen, S. Kaasalainen, and Y. Chen. 2012. "Full Waveform Hyperspectral LiDAR for Terrestrial Laser Scanning." *Optics Express* 20 (7): 7119–7127. doi:10.1364/OE.20.007119.

Hu, K., Y. Zhao, M. Ye, J. Gao, G. Zhao, and G. Zhou. 2017. "Design of a CMOS ROIC for InGaAs Self-mixing Detectors Used in FM/cw LADAR." *IEEE Sensors Journal* 17 (17): 5547–5557. doi:10.1109/JSEN.2017.2724064.

Hu, P., H. Huang, Y. Chen, J. Qi, W. Li, C. Jiang, H. Wu, W. Tian, and J. Hyyppä. 2020. "Analyzing the Angle Effect of Leaf Reflectance Measured by Indoor Hyperspectral Light Detection and Ranging (Lidar)." *Remote Sensing* 12 (6): 919. doi:10.3390/rs12060919.

Jiang, C., Y. Chen, H. Wu, W. Li, H. Zhou, Y. Bo, H. Shao, S. Song, E. Puttonen, and J. Hyyppä. 2019. "Study of a High Spectral Resolution Hyperspectral LiDAR in Vegetation Red Edge Parameters Extraction." *Remote Sensing* 11 (17): 2007. doi:10.3390/rs11172007.

Kaasalainen, S., T. Lindroos, and J. Hyyppa. 2007. "Toward Hyperspectral Lidar: Measurement of Spectral Backscatter Intensity with a Supercontinuum Laser Source." *IEEE Geoscience and Remote Sensing Letters* 4 (2): 211–215. doi:10.1109/LGRS.2006.888848.

Li, W., C. Jiang, Y. Chen, J. Hyyppä, L. Tang, C. Li, and S. W. Wang. 2019. "A Liquid Crystal Tunable Filter-Based Hyperspectral LiDAR System and Its Application on Vegetation Red Edge Detection." *IEEE Geoscience and Remote Sensing Letters* 16 (2): 291–295.32. doi:10.1109/LGRS.2018.2870143.

Li, W., G. Sun, Z. Niu, S. Gao, and H. Qiao. 2014. "Estimation of Leaf Biochemical Content Using a Novel Hyperspectral Full-waveform LiDAR System." *Remote Sensing Letters* 5 (8): 693–702. doi:10.1080/2150704X.2014.960608.

Lin, D., M. Yingying, and B. Zhu. 2014. "A Methodto Select Receiving Channels for the Multi-spectral Earth Observation LIDAR." *Acta Optica Sinica* 8: 296–303.

Luo, S., C. Wang, X. Xi, S. Nie, X. Fan, H. Chen, X. Yang, D. Peng, Y. Lin, and G. Zhou. 2019. "Combining Hyperspectral Imagery and LiDAR Pseudo-waveform for Predicting Crop LAI, Canopy Height and Above-ground Biomass." *Ecological Indicators* 102: 801–812. doi:10.1016/j.ecolind.2019.03.011.

Morsdorf, F., C. Nichol, T. Malthus, and I. H. Woodhouse. 2009. "Assessing Forest Structural and Physiological Information Content of Multi-spectral LiDAR Waveforms by Radiative Transfer Modelling." *Remote Sensing of Environment* 113 (10): 2152–2163. doi:10.1016/j.rse.2009.05.019.

Morsy, S., A. Shaker, and A. El-Rabbany. 2017. "Multispectral LiDAR Data for Land Cover Classification of Urban Areas." *Sensors* 17 (5): 958.

Muller, D., C. A. Hostetler, R. Ferrare, S. Burton, E. Chemyakin, A. Kolgotin, J. W. Hair, A. Cook, D. B. Harper, and R. Rogers. 2014. "Airborne Multiwavelength High Spectral Resolution Lidar (HSRL-2) Observations during TCAP 2012: Vertical Profiles of Optical and Microphysical Properties of a Smoke/urban Haze Plume over the Northeastern Coast of the US." *Atmospheric Measurement Techniques (Online)* 7 (PNNL-SA-100132).

Nevalainen, O., T. Hakala, J. Suomalainen, R. Mäkipää, M. Peltoniemi, A. Krooks, and S. Kaasalainen. 2014. "Fast and Nondestructive Method for Leaf Level Chlorophyll Estimation Using Hyperspectral LiDAR." *Agricultural and Forest Meteorology* 198: 250–258. doi:10.1016/j.agrformet.2014.08.018.

Nishizawa, T., N. Sugimoto, and I. Matsui. 2011. "Dual-wavelength High-Spectral-Resolution Lidar for Advanced Classification and Retrieval of Aerosols." Paper presented at the 2011 IEEE International Geoscience and Remote Sensing Symposium, 4157–4160, July, Vancouver, BC.

Niu, Z., Z. Xu, G. Sun, W. Huang, L. Wang, M. Feng, W. Li, W. He, and S. Gao. 2015. "Design of a New Multispectral Waveform LiDAR Instrument to Monitor Vegetation." *IEEE Geoscience and Remote Sensing Letters* 12 (7): 1506–1510. doi:10.1109/LGRS.2015.2410788.

Puttonen, E., C. Briese, G. Mandlburger, M. Wieser, M. Pfennigbauer, A. Zlinszky, and N. Pfeifer. 2016. "Quantification of Overnight Movement of Birch (Betula Pendula) Branches and Foliage with Short Interval Terrestrial Laser Scanning." *Frontiers in Plant Science* 7: 222. doi:10.3389/fpls.2016.00222.

Puttonen, E., T. Hakala, O. Nevalainen, S. Kaasalainen, A. Krooks, M. Karjalainen, and K. Anttila. 2015. "Artificial Target Detection with a Hyperspectral LiDAR over 26-h Measurement." *Optical Engineering* 54 (1): 013105. doi:10.1117/1.OE.54.1.013105.

Qin, H., C. Wang, X. Xi, S. Nie, and G. Zhou. 2018. "Integration of Airborne LiDAR and Hyperspectral Data for Maize FPAR Estimation Based on a Physical Model." *IEEE Geoscience and Remote Sensing Letters* 15 (7): 1120–1124. doi:10.1109/LGRS.2018.2825878.

Qin, H., C. Wang, X. Xi, J. Tian, and G. Zhou. 2017a. "Estimation of Coniferous Forest Aboveground Biomass with Aggregated Airborne Small-footprint LiDAR Full-waveforms." *Optics Express* 25 (16): A851–A869. doi:10.1364/OE.25.00A851.

Qin, H., C. Wang, X. Xi, J. Tian, and G. Zhou. 2017b. "Simulating the Effects of the Airborne Lidar Scanning Angle, Flying Altitude, and Pulse Density for Forest Foliage Profile Retrieval." *Applied Sciences* 7 (7): 712. doi:10.3390/app7070712.

Rall, J. A., and R. G. Knox. 2004. "Spectral Ratio Biospheric Lidar." Paper presented at the IGARSS 2004. 2004 IEEE International Geoscience and Remote Sensing Symposium, Matera, Italy, 3, 1951–1954.

Rao, Z.-M., T.-Y. He, D.-X. Hua, and R.-X. Chen. 2018. "Remote Sensing of Particle Mass Concentration Using Multi-wavelength Lidar." *Spectroscopy and Spectral Analysis* 38 (4): 1025–1030.

Schlemmer, M., A. Gitelson, J. Schepers, R. Ferguson, Y. Peng, J. Shanahan, and D. Rundquist. 2013. "Remote Estimation of Nitrogen and Chlorophyll Contents in Maize at Leaf and Canopy Levels." *International Journal of Applied Earth Observation and Geoinformation* 25: 47–54. doi:10.1016/j.jag.2013.04.003.

Shao, H., Y. Chen, Z. Yang, C. Jiang, W. Li, H. Wu, Z. Wen, S. Wang, E. Puttonen, and J. Hyyppä. 2019. "A 91-Channel Hyperspectral LiDAR for Coal/Rock Classification." *IEEE Geoscience and Remote Sensing Letters* 17 (6): 1052–1056. doi:10.1109/LGRS.2019.2937720.

Sun, G., Z. Niu, S. Gao, W. Huang, L. Wang, W. Li, and M. Feng. 2014. "32-channel Hyperspectral Waveform LiDAR Instrument to Monitor Vegetation: Design and Initial Performance Trials." Paper presented at the Multispectral, Hyperspectral, and Ultraspectral Remote Sensing Technology, Techniques and Applications V, Beijing, China.

Sun, J., S. Shi, W. Gong, J. Yang, L. Du, S. Song, B. Chen, and Z. Zhang. 2017. "Evaluation of Hyperspectral LiDAR for Monitoring Rice Leaf Nitrogen by Comparison with Multispectral LiDAR and Passive Spectrometer." *Scientific Reports* 7: 40362. doi:10.1038/srep40362.

Suomalainen, J., T. Hakala, H. Kaartinen, E. Räikkönen, and S. Kaasalainen. 2011. "Demonstration of a Virtual Active Hyperspectral LiDAR in Automated Point Cloud Classification." *ISPRS Journal of Photogrammetry and Remote Sensing* 66 (5): 637–641. doi:10.1016/j.isprsjprs.2011.04.002.

Swatantran, A., R. Dubayah, D. Roberts, M. Hofton, and J. B. Blair. 2011. "Mapping Biomass and Stress in the Sierra Nevada Using Lidar and Hyperspectral Data Fusion." *Remote Sensing of Environment* 115 (11): 2917–2930. doi:10.1016/j.rse.2010.08.027.

Teledyne Optech—Titan Brochure and Specifications. 2015. "Optech Titan Multispectral LiDAR System—High Precision Environmental Mapping." Accessed 30 July 2020. http://www.teledyneoptech.com/wp-content/uploads/Titan-Specsheet-150515-WEB.pdf

Wei, G., S. Shalei, Z. Bo, S. Shuo, L. Faquan, and C. Xuewu. 2012. "Multi-wavelength Canopy LiDAR for Remote Sensing of Vegetation: Design and System Performance." *ISPRS Journal of Photogrammetry and Remote Sensing* 69: 1–9. doi:10.1016/j.isprsjprs.2012.02.001.

Wirth, M., A. Fix, P. Mahnke, H. Schwarzer, F. Schrandt, and G. Ehret. 2009. "The Airborne Multi-wavelength Water Vapor Differential Absorption Lidar WALES: System Design and Performance." *Applied Physics B* 96 (1): 201. doi:10.1007/s00340-009-3365-7.

Yang, J., B. Huang, Z. Zhang, and S. Yin. 2013. "Simulation Study of Detecting Various Gases Based on Far-infrared Wide Spectrum LiDAR ." *Laser & Infrared* 43 (7): 743–746.

Zhou, G., and X. Zhou. 2018. *Technology and Applications for Array LiDAR Imager*. Wuhan Univ. Press, Wuhan, China.

Zhou, G., X. Zhou, J. Yang, Y. Tao, X. Nong, and O. Baysal. 2015. "Flash Lidar Sensor Using Fiber-coupled APDs." *IEEE Sensors Journal* 15 (9): 4758–4768. doi:10.1109/JSEN.2015.2425414.